Construction and Building Materials xxx (xxxx) 128686

Contents lists available at ScienceDirect

Construction and Building Materials

journal homepage: www.elsevier.com/locate/conbuildmat

Effect of borax on the hydration and setting of magnesium phosphate cements

Rita Gelli [a, 1], Monica Tonelli [a, 1], Francesca Martini [b, c], Lucia Calucci [c, d], Silvia Borsacchi [c, d, *], Francesca Ridi [a, *]

[a] Department of Chemistry "Ugo Schiff" and CSGI, University of Florence, via della Lastruccia 3, 50019 Sesto Fiorentino, Florence, Italy
[b] Department of Chemistry and Industrial Chemistry, University of Pisa, via G. Moruzzi 13, 56124 Pisa, Italy
[c] Center for Instrument Sharing of the University of Pisa (CISUP), 56126 Pisa, Italy
[d] Institute for the Chemistry of OrganoMetallic Compounds-ICCOM, Italian National Research Council-CNR, via G. Moruzzi 1, 56124 Pisa, Italy

ARTICLE INFO

Keywords:
Magnesium phosphate cements
Tri-magnesium phosphate
Borax
Retarders
Setting
Kinetics
Solid state NMR

ABSTRACT

This work unravels for the first time the concentration dependent retarding effect of borax on tri-magnesium phosphate-based cements by studying the hydration and the phases formed in the set cements, exploiting multiple characterization techniques. In the presence of borax, the hydration was found to be slower and less exothermic, leading to the formation of struvite without newberyite, with no effect on cement's strength. The observed boron species allowed us to ascribe the retardation to the complexation of NH_4^+ and Mg^{2+} by borate and polyborate anions.

1. Introduction

Magnesium Phosphate-based cements (MPCs) have recently gained a renewed interest in a variety of fields including the repair of concrete elements, the stabilization of radioactive wastes, water treatment and biomedical applications [1–5]. MPCs are typically prepared by mixing a powder component (MgO or TMP, Tri-Magnesium Phosphate, $Mg_3(PO_4)_2$) with an aqueous solution of a phosphate salt, such as mono- or di-ammonium hydrogen phosphate, di-sodium hydrogen phosphate, di-potassium hydrogen phosphate, or phosphoric acid. Upon mixing, the dissolution of the powder and its reaction with the ions in the phosphate salt solution give a moldable paste, due to the formation of new phases in the cement matrix. In time, the newly formed crystals entangle and form a network which leads to the setting of the paste producing a hard and compact cement matrix. Depending on the type and amount of reactants, a variety of phases can form during the setting process and in the final cement, struvite ($MgNH_4PO_4{\cdot}6H_2O$) being the most common [6].

MPCs are endowed with a series of properties, which make them attractive for several applications. In the construction field, MPCs are appealing due to their early strength, fast setting, good durability and favorable bonding strength with old concrete [1]. For biomedical applications, these materials are promising as bone cements thanks to their favorable combination of setting time, mechanical properties and resorption rate, as well as for their ability to release Mg^{2+}, which promotes bone regeneration [3].

For the preparation of MPCs, the majority of literature studies take advantage of MgO as a starting material [4]. The use of TMP is mainly restricted to the development of materials for orthopedic applications [7–15], also prepared by 3D printing [16–19]. These studies are in general mainly focused on the characterization of the final cement matrix and on its biological performances rather than on the mechanism and kinetics of phases' formation. Nevertheless, understanding the setting process in such materials would be important to gain insights into the hydration mechanisms of cements based on TMP and to develop strategies to improve their performances. Even if no direct comparison of

Abbreviations: MPCs, magnesium phosphate cements; TMP, tri-magnesium phosphate; RT, room temperature; RH, relative humidity; DSC, differential scanning calorimetry; XRD, X-ray diffraction; FE-SEM, field emission scanning electron microscopy; NMR, nuclear magnetic resonance; SS NMR, solid state NMR; DE, direct excitation; CP-MAS, cross polarization-magic angle spinning

* Corresponding authors at: Institute for the Chemistry of OrganoMetallic Compounds-ICCOM, Italian National Research Council-CNR, via G. Moruzzi 1, 56124 Pisa, Italy (S. Borsacchi).
E-mail addresses: silvia.borsacchi@pi.iccom.cnr.it (S. Borsacchi), francesca.ridi@unifi.it (F. Ridi).
[1] These authors equally contributed to the work.

https://doi.org/10.1016/j.conbuildmat.2022.128686
Received 23 May 2022; Received in revised form 26 July 2022; Accepted 3 August 2022
0950-0618/

MgO and TMP-based cements is reported in the literature, the use of TMP over MgO should lead to the following advantages: *i.* No release of ammonia during setting, which may create unpleasant odor and favor corrosion [20,21]; *ii.* Smaller increase in pH during setting, which is attractive for radioactive waste storage applications [5,22,23]; *iii.* Less exothermic setting reaction, important to avoid tissue necrosis in biomedical applications. The setting mechanism of MgO-based cements is, on the other hand, well investigated in the literature, both from an experimental and a theoretical perspective [6,24–28].

An aspect so far neglected in TMP-based MPCs is the addition of retarders, which are typically used in MgO-based systems to control the intensity of the exothermic reactions and the setting time of MPCs pastes [1]. A thorough understanding of the retarders and their action mechanism is fundamental to modulate the properties of MPCs and to extend their field of application. For MgO-based systems, a library of retarders has been tested, including acetic acid [29,30], citrate [31], sodium triphosphate [32,33], and, in particular, borax/boric acid [6, 33–37]. Borax is by far the most used and the most effective additive; notwithstanding, in the literature there is no consensus on the mechanism of action in retarding the setting of MgO-based MPCs [6,38]. Sugama and Kukacka first hypothesized that, when mixed with phosphate, borax is hydrolyzed in the solution to yield $B_4O_7^{2-}$ ions, which react with Mg^{2+} on MgO grains to produce a compound that precipitates as a film around the MgO grains, retarding the reaction between MgO and phosphate [39]. Wagh et al. identified a coating on MgO particles as Lünebergite ($Mg_3B_2(PO_4)_2(OH)_6{\cdot}6H_2O$) [28], while Lahalle et al. indicated that the retardation mechanism of boric acid in the formation of K-struvite ($MgKPO_4$) from MgO and KH_2PO_4 can be attributed to the formation of an amorphous mineral containing borate and orthophosphate and to the stabilization of Mg^{2+} and K^+ ions in solution to counterbalance the negative charge of polyborates formed [40]. Another study hypothesizes that, in MPCs based on K-struvite, borax forms a film onto the surface of MgO grains, decreasing the temperature during setting and increasing the pH of the system [41].

On the other hand, the use of retarders for TMP-based MPCs has not been extensively investigated yet. A few reports describe the use of retarders for TMP-based cements, *i.e.,* citrate [42] and phytic acid [43]. The use of borax, the most effective retarder for MgO-based MPCs, has not been reported yet for TMP-based MPCs. In this work, we have analyzed in detail the effect of borax and, by exploiting several characterization techniques, we have investigated its mechanism of action.

Understanding borax's action mechanism on MPCs is also important for evaluating their potential toxicity. In fact, despite borax being used since decades in a variety of fields, including food, medicine and cosmetics, some concerns about its toxicity for reproduction have been recently raised [44]. Even so, this additive is still extensively used in MgO-based cements, and assessing if it can exert a retarding action also in TMP-based systems and understanding in which form it is included in the final cement matrix is of utmost importance to define the hydration mechanism and to evaluate the potential toxicity of the materials.

In this work, we investigated for the first time the effect of borax on TMP-based MPCs, in the attempt of clarifying the interactions taking place in the retarding mechanism. The impact of different concentrations of borax on both the setting mechanism and the final properties of TMP-based cements was thoroughly assessed by combining different characterization techniques. The setting time of the pastes was measured by means of the Gillmore test, whereas differential scanning calorimetry was used to monitor the heating evolution. The kinetics of phases' formation was followed by means of confocal Raman microscopy, and the pH during the setting reaction was also measured. Set cements were also analyzed in terms of morphology, phases' composition and mechanical properties by exploiting Field Emission-Scanning Electron Microscopy, X-ray Diffraction, Compressive Tests and Solid State NMR spectroscopy for the observation of ^{31}P and ^{11}B nuclei [40, 45,46]. The release of boron from the cement matrix upon incubation in water was also assessed. This multi-technique approach allowed us to unravel the effect of borax on both the cement formation reaction and on the final product, as well as hypothesizing its action mechanism on TMP-based cements at a structural level.

2. Materials and methods

2.1. Materials

Magnesium hydroxide ($Mg(OH)_2$, purity > 95 %) was purchased from Fluka, newberyite ($MgHPO_4{\cdot}3H_2O$, purity > 97 %) was obtained from Sigma-Aldrich, while di-ammonium hydrogen phosphate ($(NH_4)_2HPO_4$, DAHP, purity > 99 %) was supplied by Riedel de Haën. Sodium tetraborate decahydrate (borax, $Na_2B_4O_7{\cdot}10H_2O$, purity > 99 %) was purchased from Alfa Aesar. Milli-Q water was used throughout all the experiments. All materials were used as received, without any further purification.

2.2. Preparation of cements with different amounts of borax

Cements were prepared by mixing TMP with aqueous solutions of DAHP, which react producing struvite ($MgNH_4PO_4{\cdot}6H_2O$) and newberyite ($MgHPO_4{\cdot}3H_2O$) [42]:

$$Mg_3(PO_4)_2 + (NH_4)_2HPO_4 + 15H_2O \rightarrow 2MgNH_4PO_4{\cdot}6H_2O + MgHPO_4{\cdot}3H_2O$$

TMP was prepared by means of a calcination reaction by heating at 1000 °C $Mg(OH)_2$ and $MgHPO_4{\cdot}3H_2O$ in a 1:2 mol:mol ratio (procedure thoroughly described elsewhere [47]). The purity and the size distribution of the product were confirmed by XRD pattern and laser granulometry as shown in Fig. S1. Cements containing different amounts of borax were prepared according to the compositions in Table 1. TMP and borax were weighted and, after carefully mixing the powders for 1 min with a spatula, a 3.5 M DAHP aqueous solution was added to form the paste (TMP to liquid ratio 1.5 g/mL). After about 30 s of mixing with a spatula, the appearance of the paste was observed (see Section 3.2); afterwards the paste was transferred in a cylindrical plastic mold (diameter: 1 cm) and allowed to set at room temperature (RT) and controlled relative humidity (RH > 96 %).

2.3. Cements characterization

2.3.1. Setting time

The initial and final setting times of the cement pastes containing different amounts of borax were determined by means of a Gillmore apparatus (Matest, Bergamo, Italy), following the C-266 ASTM standard. Fresh pastes were prepared according to the compositions in Table 1 and placed in plastic molds. Samples were kept at RT and RH > 96 % for the whole duration of the experiment and, every 5 min, their surface was tested with the Gillmore apparatus. The cement is considered to have attained its initial (t_1) or final (t_2) setting time when its surface respectively bears the initial or final Gillmore needle without appreciable indentation (initial needle diameter: 2.12 mm, weight 113.4 g and final needle diameter: 1.06 mm, weight 453.6 g). The error bars associated with the measurements (±5 min) correspond to the used sampling interval.

Table 1
Composition of the prepared cements.

Sample	TMP (g)	3.5 M DAHP (mL)	Borax (g)	Borax/TMP wt%
B0	0.5	0.333	0	0
B2	0.5	0.333	0.01	2
B5	0.5	0.333	0.025	5
B10	0.5	0.333	0.05	10

2.3.2. Differential scanning calorimetry (DSC)

DSC was used to monitor the heat flow released during the setting reaction of MPCs containing different amounts of borax. Measurements were carried out using a DSC Q2000 (TA Instruments, New Castle, DE, USA). For the experiment, samples were prepared by mixing 50 mg of TMP with 0 mg, 1 mg, 2.5 mg, or 5 mg of borax for samples B0, B2, B5, and B10, respectively, and adding 33 μL of 3.5 M DAHP solution. Each paste was quickly mixed and placed in T0 Al Hermetic pans (TA Instruments) for the measurement. The hermetically sealed pans were subjected to an isothermal scan at 25 °C for 16 h.

2.3.3. Confocal Raman microscopy

The setting kinetics of the cement pastes B0 and B10 was studied by means of confocal Raman analysis. Measurements were conducted on a Renishaw inVia Qontor confocal MicroRaman system using a 785 nm laser, a front illuminated CCD camera and a research-grade Leica DM 2700 microscope equipped with a 5X objective (NA 0.12, WD 14 mm). Samples were prepared by mixing 150 mg of TMP (together with 15 mg of borax for B10) with 100 μL of 3.5 M DAHP and were immediately placed in a mold under the microscope's objective. Spectra of the pastes surface were collected after 3 min, 6 min, 10 min, 20 min, 30 min, 1 h, 2 h, 3 h, 4 h, 5 h, and 24 h using 100 % laser power (100 mW), 10 s exposure time, 3 accumulations in the range 150–1350 cm^{-1}. Each spectrum was processed with baseline subtraction and smoothing. Signals were discussed by comparing the experimental spectra with those of the powdered pure phases constituting our samples (TMP, struvite, and newberyite), which were collected using a 20X objective, 10 % laser power, 10 s *per* spectrum, and 3 accumulations. For TMP, the powder used to prepare the cements was tested, while for newberyite the commercial product (see 2.1) was analyzed. A pure struvite sample was synthesized following a protocol from the literature [48] (see the preparation in the Supplementary Material) and its structure was checked by XRD (see Fig. S2) and ^{31}P Solid State NMR (see Results and Discussion).

2.3.4. pH measurements

The pH of the pastes B0 and B10 was tested during the setting process with a protocol typically used for cements forming magnesium silicate hydrate [49]. 0.5 g of TMP (together with 0.05 g of borax in the case of B10) were mixed with 0.333 mL of a 3.5 M DAHP aqueous solution and an excess of H_2O (5 mL). At selected time intervals (2 min, 5 min, 15 min, 30 min, 1 h, 2 h, 3 h, 5 h, 8 h, 24 h, 48 h, 72 h, 6 days, and 9 days) samples were mixed with vortex for about 10 s, centrifuged at 2000 rpm to precipitate the paste (Hettich, EBA 20 centrifuge), and then the pH of the supernatant was measured with a pH meter (pH 7 + DHS, XS Instruments). Between measurements, samples were kept oscillating in an orbital shaker (Standard Analog shaker, VWR) at RT.

To support the relationship between pH values and cement hydration, the experiment was repeated in the same conditions and 1 mL aliquots were collected after 2 min, 30 min, 5 h, and 4 days. Aliquots were withdrawn, centrifuged for 1 min and the precipitate was immediately analyzed by means of confocal Raman microscopy. Spectra were collected using the instrument described in Section 2.3.3, with a 785 nm laser operating at 100 % power (100 mW), exposure time 10 s, 3 accumulations, in the spectral range 150–1350 cm^{-1}.

2.3.5. X-ray diffraction (XRD)

XRD data were collected with a D8 Advance with DAVINCI design (Bruker, Milan, Italy), using as X-rays source the Cu Kα radiation (wavelength $\lambda = 1.542$ Å), at 40 kV and 40 mA, a 2θ range of 10 – 60°, a step size of 0.03°, and a time/step of 0.3 s. Before the analysis, set cements were ground with mortar and pestle and flattened on a Si zero-background sample holder. Peaks' assignment was based on the Powder Diffraction Files (PDF) of the database of the International Centre for Diffraction Data.

2.3.6. Field emission-scanning electron microscopy (FE-SEM)

FE-SEM images were collected on cements' cross-sections with a field-emission ΣIGMA microscope (Carl Zeiss Microscopy, Germany). Specimens were fixed on aluminum stubs by means of conductive tape. The accelerating potential was 2.00 kV, with a ~4 mm working distance. Images were acquired using an InLens detector.

2.3.7. Compressive strength

The compressive strength of set cements (B0 and B10) was tested by performing a compression analysis with an electromechanical universal testing machine Instrom 5500 L with a 10 kN load cell. B0 was prepared by mixing 2.4 g of TMP with 1.6 mL of 3.5 M DAHP solution, and B10 was prepared by mixing 2.4 g of TMP with 0.24 g borax and then adding 1.6 mL of 3.5 M DAHP solution. The pastes were poured in cylindrical molds (diameter 13 mm, height ~13 mm) and set at RT and RH > 96 % for 5 days. The specimens were extracted from the molds and polished with abrasive paper to obtain an aspect ratio of about 1 (height/diameter), making the two surfaces of the cylinders as flat as possible, in order to be sure that all specimens had the same dimensions. Five samples were prepared for each composition; results are reported as average ± standard deviation.

2.3.8. Solid State NMR (SS NMR) spectroscopy

SS NMR spectroscopy was applied to investigate set B0 and B10 cements and reference samples TMP, newberyite, struvite and Lüneburgite (see Supplementary Material for the preparation of struvite and Lüneburgite and Figs. S3 and S4 for characterization). Solid State NMR spectra were recorded on a Bruker Avance Neo 500 spectrometer, working at Larmor frequencies of 202.46 and 160.46 MHz for ^{31}P and ^{11}B, respectively, with a Cross Polarization-Magic Angle Spinning (CP-MAS) probehead accommodating rotors with outer diameter of 4 mm. ^{31}P spectra were recorded using a Direct Excitation (DE) pulse sequence, under MAS at a frequency of 15 kHz and under High Power Decoupling from ^{1}H nuclei. For TMP and set B0 and B10 samples, quantitative ^{31}P spectra were recorded by applying a 90° excitation pulse and a recycle delay between two consecutive transients of 2000 s, determined after suitable calibration. 4 and 44 transients were accumulated for TMP and cement samples, respectively. The ^{31}P chemical shift scale was referred to the signal of H_3PO_4 80 % at 0 ppm. The ^{11}B spectrum of B10 was recorded at a MAS frequency of 13 kHz, using a DE pulse sequence and, for obtaining quantitative spectra, an excitation pulse corresponding to a very small tip angle (about 10°), a recycle delay of 5 s and accumulating 7040 transients. All experiments were carried out at room temperature and exploiting air as spinning gas.

The simulated ^{11}B MAS spectrum was computed as the sum of individual lines using the Dmfit program [50]. For each line, the QMAS-1/2 model was employed, which simulates second order quadrupolar lineshapes related to the central transition of half-integer quadrupolar nuclei under infinitely high MAS rate. The model provided the values of the isotropic chemical shift, of the quadrupolar coupling constant (C_Q), and asymmetry parameter (η) of the quadrupolar coupling tensor for boron sites.

2.4. Release of boron from the cements

Samples B0 and B10 for the release experiment were prepared by mixing 0.3 g of TMP with 200 μL of 3.5 M DAHP solution (in case of B10, TMP was mixed with 0.03 g of borax). The pastes were poured in a plastic mold (diameter 8 mm) and set at RT and RH > 96 % for one week. For the release experiment, MPCs were removed from the mold and placed on a metallic grid which was suspended in a plastic test tube containing 10 mL of Milli-Q water. A magnetic stirrer was also placed in the test tube, to ensure homogeneity of the incubating medium. The experiment was conducted at RT and 1 mL aliquots were collected after 1 h, 8 h, 24 h, 3 days, 7 days, 14 days, 21 days, and 28 days. After each

withdrawal, 1 mL of Milli-Q water was added to the system, to keep the volume constant. For B10, the experiment was conducted in triplicate, and the results are expressed as average ± standard deviation. Sample B0 incubated for 7 days was also analyzed as a reference.

The amount of boron in the samples was measured in triplicate by means of an Agilent 720-ES Inductively Coupled Plasma Atomic Emission Spectrometer (ICP-OES) equipped with a pneumatic nebulizer and a cyclonic spray chamber. Before the analyses, 500 μL of each sample was diluted to 5 mL with ultrapure water and then 1.0 ppm of Ge was added, as an internal standard to correct any matrix effect. The calibration curves were obtained using standard solutions prepared from commercial standards certified at 1000 ppm. The analytical line used for B quantification was at 208.956 nm while the Ge line used for the correction was at 209.426 nm. After each measurement, the system was washed with a 2 % HNO_3 solution.

3. Results and discussion

3.1. Effect of borax on the setting mechanism of TMP-based MPC

The effect of borax on TMP-based MPC hydration was initially evaluated by observing the appearance of the pastes after mixing (see Fig. 1A). Borax has a concentration-dependent liquefying effect on the paste, thus affecting its consistency and handling properties. This observation was correlated with the setting times measured with the Gillmore apparatus. The results, reported in Fig. 1B and Table S1, show that pastes without borax set in few minutes (t_1 = 10 min, t_2 = 15 min), consistently with data reported in the literature for other MPCs [42,47]. The inclusion of borax in the formulation allows extending and, most importantly, tuning the setting time according to the concentration used: the plot in Fig. 1C reveals a linear correlation between both the initial and the final setting times and the borax content in the mixture. The obtained good linear dependence (R^2 = 0.993) suggests

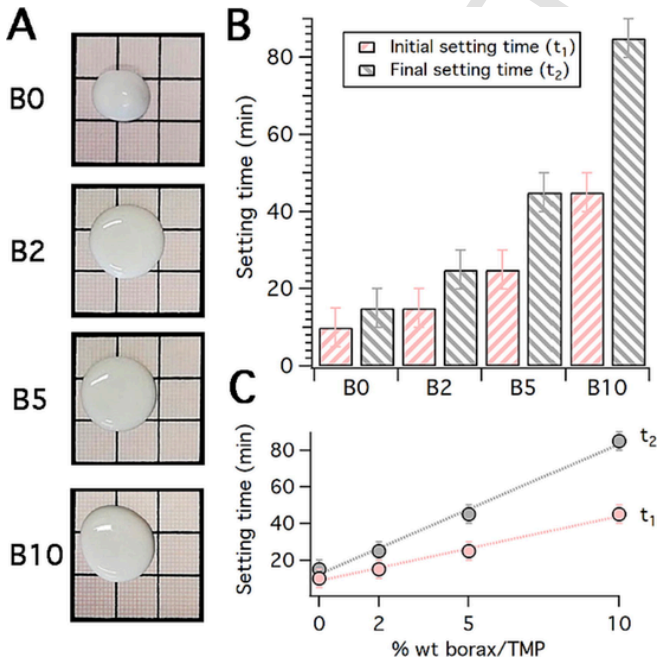

Fig. 1. A) Photos of the pastes 30 s after the beginning of mixing. The amount of borax increases from the top to the bottom. Each photo is 3 cm × 3 cm; B) Initial (t_1, pink) and final (t_2, grey) setting times obtained from the Gillmore test; C) Plot of the initial and final setting times as a function of borax content in the formulations and linear fittings (dashed lines). For t_1, the obtained equation is y = 8.7 + 3.5x (R^2: 0.993), for t_2 y = 12.4 + 7.1x (R^2: 0.993). (For interpretation of the references to colour in this figure legend, the reader is referred to the web version of this article.)

that TMP-based cements with a desired setting time can be obtained by simply controlling the borax content in the formulation: this is particularly important as the fast setting of MPCs, which is one of their main characteristics [1], may hamper those applications where a certain handling time is needed before paste application [36].

The setting reaction of the pastes was further analyzed by means of differential scanning calorimetry. Immediately after mixing, the pastes were loaded in the instrument and the heat flow during an isothermal step at 25 °C was monitored for 16 h. The obtained curves are shown in Fig. 2. For B0, a strong and narrow exothermic event occurs after 21 min of setting, followed by a small peak at 71 min, suggesting a multi-step process. The presence of borax in the formulations delays and weakens the exothermic peak, as already observed for cements based on K-struvite [34]. For B10, a distinct exothermic peak is not visible but a low and constant heat flow release occurs up to about 150 min. The plot of peak's maximum vs borax percentage in the samples shows a linear trend (see the inset in Fig. 2).

The heat release that occurs during setting is connected to the exothermicity of the reaction, which is well-known for MPCs prepared with MgO as starting material. Here, we demonstrate that also in the case of TMP-based MPCs, the setting of the paste is connected to a heat release, this event being affected by borax. This additive slows down the setting reaction and makes it less violent, as it is demonstrated by the shift in time and the decrease in intensity of the exothermic peak.

It is worth noting that in the heat flow profiles the peaks show their maximum at time values longer than the final setting times obtained by means of the Gillmore test (see the comparison in Table S1). Nevertheless, t_2 does not necessarily corresponds to the end of the setting reaction, but rather to the obtainment of a specific degree of paste hardening. The evolution of the phases in the cement pastes might extend to a longer time, due to dissolution and reprecipitation processes of the crystalline phases that lead to the formation of the final material.

In order to further inspect the kinetics of the phases' formation and the effect of borax, the pastes were analyzed by means of confocal Raman microscopy during setting. The kinetics of phases' formation in TMP-based cement is often neglected in the literature; in this work we propose for the first time the use of confocal Raman microscopy for its assessment. With this technique, Raman spectra of untreated samples' surface can be collected in short times, even in the early stages of setting when samples are in the form of pastes, allowing one to follow the rapid evolution of these materials. It is worth mentioning that, since stopping the hydration is not required for the use of confocal Raman, it

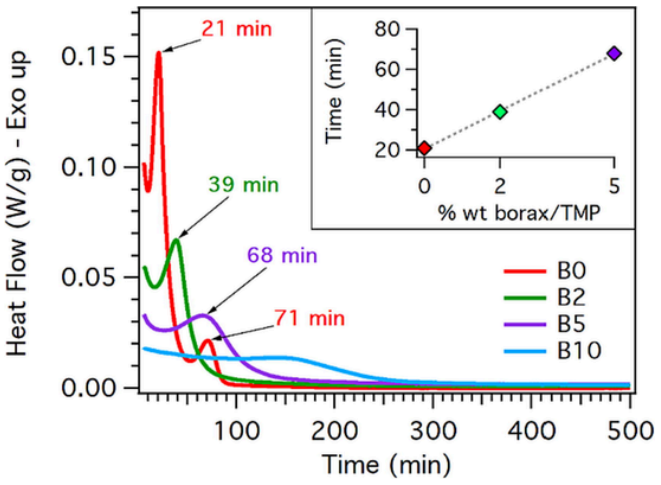

Fig. 2. DSC curves of fresh pastes at different borax content (red B0, green B2, purple B5 and blue B10). In the inset, plot of the time of peak's maximum vs amount of borax in the formulations, and linear fitting of the trend (dashed line). (For interpretation of the references to colour in this figure legend, the reader is referred to the web version of this article.)

is possible to avoid any manipulation that could affect the samples. According to the reaction shown in Section 2.2, TMP reacts with DAHP forming struvite ($MgNH_4PO_4{\cdot}6H_2O$) and newberyite ($MgHPO_4{\cdot}3H_2O$) as final setting materials. Unreacted TMP should also be present in the final matrix, as the cement formation reaction occurs due to dissolution and precipitation processes around TMP, which is in excess with respect to DAHP [4]. First, the spectra of the phases expected to be present in the cement were collected to be taken as references for the analysis of pastes spectra; the results are shown in Fig. 3A. The evolution of the pastes was then assessed by collecting spectra during the setting process. As a representative example, the spectra of B0 and B10 after 30 min of setting (B0_30 min and B10_30 min) are shown in Fig. 3B. For B0 we can observe signals compatible with TMP (main features at 982 cm^{-1}, 1029 cm^{-1}, and 1058 cm^{-1}) and struvite (564 cm^{-1} and 945 cm^{-1}). The shoulder at ~ 900 cm^{-1} is compatible with the presence of a small amount of newberyite, whose most intense peak is superimposed to that of TMP at 982 cm^{-1}. Concerning the spectrum of B10, almost all signals can be ascribed to TMP, as only a very weak and broad band is observed at 945 cm^{-1}, suggesting a low conversion degree to struvite after 30 min. The small signal at 878 cm^{-1}, present only for B10 at short times of setting (see Fig. 3B), is compatible with transient borate species formed during the setting process, such as Lüneburgite (see Fig. S5 in the Supplementary Material), as sometimes suggested in the literature for MgO-based systems [28]. The setting kinetics of the pastes was followed by monitoring the evolution of struvite main peak at 945 cm^{-1}, as it is shown in Fig. 3C. For B0, a very small signal is already present after 3 min of setting, and it increases abruptly from 30 min to 1 h, reaching a plateau. In contrast, for B10 no appreciable peaks are visible in this region up to about 30 min; afterwards, the intensity of the struvite signal rises gradually up to 5 h. These data demonstrate that, when no borax is present in the mixture, struvite formation takes place rapidly, whereas, in the presence of borax, struvite formation process begins later in time and it is slower and more gradual. This was further confirmed by observing the plot of struvite's peak intensity at 945 cm^{-1} as a function of time (see Fig. 3D), which was fitted with a sigmoidal function. The results of the fitting, reported in Table S2, show that in B10 the time of the inflection point of the curve is more than twofold that of B0 (0.56 ± 0.02 h for B0 and 1.86 ± 0.14 h for B10), confirming that struvite formation is delayed in the presence of borax. Moreover, the obtained k, proportional to the rise velocity (6.7 ± 1.4 h^{-1} for B0 and 1.2 ± 0.2 h^{-1} for B10), confirms that struvite formation is slowed down when borax is present in the system. The obtained results can be correlated with DSC curves shown in Fig. 2: the exothermic event for sample B0 ceases in about 80 min, while for B10 the curve returns to the baseline after about 300 min. The relatively small discrepancies between DSC and Raman timescales can be ascribed to the different setting conditions (hermetically sealed aluminum pan for DSC and plastic mold at ambient conditions for Raman).

We can conclude that confocal Raman microscopy is very effective in monitoring the setting kinetics of cements directly on pastes, without the need of stopping the setting reaction. This is of paramount importance as preliminary experiments performed on our samples showed that, in our system, procedures to arrest the setting reaction, such as freeze-drying and solvent-exchange methods, might alter the formed phases or not be effective in immediately stopping the setting (data not shown).

Fig. 4 reports the measurement of tpH during the setting process: the results show an initial pH value around 8.3 for B0 and 8.8 for B10. In B0 the pH starts to decrease after about 5 min, while in B10 it is stable up to about 2 h. Again, this is in line with the retarding effect of borax, which delays the beginning of the reaction between DAHP and TMP. Both samples, after reaching a minimum pH value (pH 6.4 at 3 h for B0 and pH 6.9 at 7 h for B10), slowly regain the initial value. Indeed, the pH values attain a plateau after about 24 h in B0 and after 6 days in B10. Therefore, the timescales in which pastes reach a stationary situation are much longer for pH than for properties investigated by other characterization techniques. For instance, with confocal Raman analysis a stationary situation was reached in 1 h for B0 and in 5 h for B10. The significant delays in time found for pH variations can be attributed to the experiment methodology. The excess of water, necessary for the measurement of the supernatant pH, dilutes the system, likely inducing a slower reaction [51]. Nonetheless, it is reasonable to infer that the observed pH variations also occur in the pastes, but on shorter time scales, and that the considerations drawn are meaningful of the original system. We can hypothesize that in the early stages of the reaction the pH of the suspension is mainly due to the DAHP solution (the measured pH of the 3.5 M DAHP solution is 8.2 at RT) and, in B10, also to the dissolution of borax. In fact, the higher pH for B10 than for B0 can be ascribed to borax hydrolysis, [52], which yields a pH of 9.13.

We can speculate that water wets the surface of TMP grains, leading to a slow dissolution process and to a release of Mg^{2+} and PO_4^{3-} ions, which surround undissolved TMP grains (it is worth noting that TMP has a solubility constant K with $\log K = -23.50$ [53]). Mg^{2+} ions then react with ammonium and phosphate ions from DAHP to form struvite ($MgNH_4PO_4{\cdot}6H_2O$) and, to a smaller extent, with hydrogen phosphate

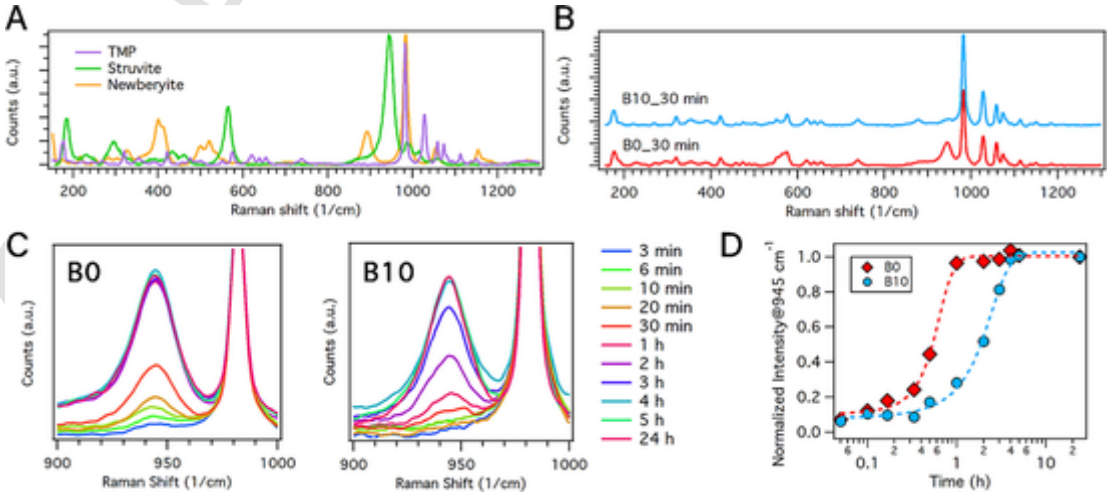

Fig. 3. A) Raman spectra of the reported pure phases; B) Raman spectra of samples B0 (bottom) and B10 (top) after 30 min of setting. The spectra are offset for display purposes; C) Raman spectra (region 900–1000 cm^{-1}) of samples B0 (left) and B10 (right) collected during setting. The spectra were normalized with respect to the most intense signal of the spectrum (982 cm^{-1}). D) Plot of the intensity at 945 cm^{-1} (struvite's most intense peak) vs time, normalized at the plateau value. Dashed lines represent sigmoidal fittings (see Supplementary Material, Table S2).

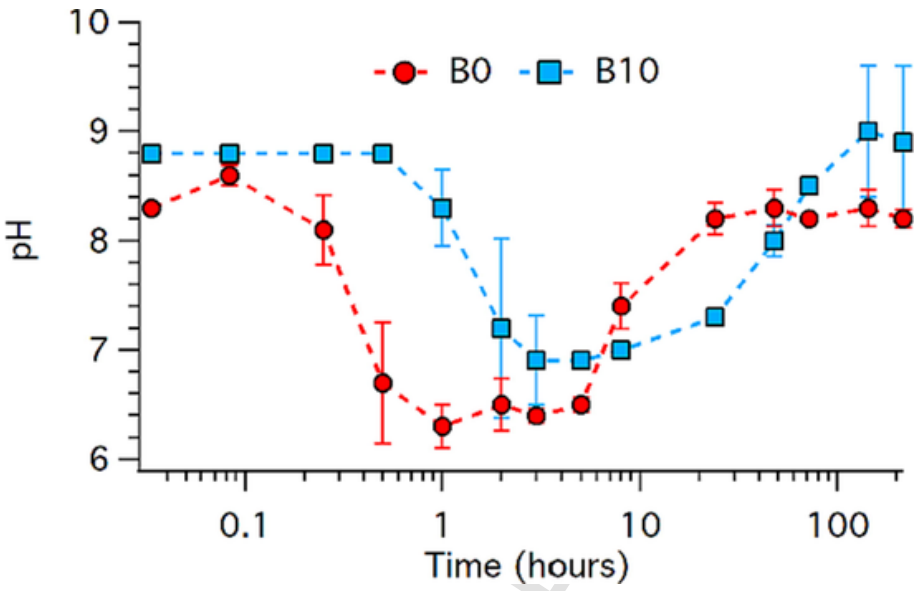

Fig. 4. pH evolution during setting for samples B0 (red dots) and B10 (blue squares). (For interpretation of the references to colour in this figure legend, the reader is referred to the web version of this article.)

resulting in newberyite ($MgHPO_4{\cdot}3H_2O$). Given that in struvite phosphates are incorporated as PO_4^{3-}, the HPO_4^{2-} ions from DAHP need to lose a H^+ to form such phase, thus decreasing the pH of the system. The observed acidification of the cement pastes during setting could thus be connected to struvite formation. Such speculations were confirmed by collecting aliquots from the pH experiments as described in Section 2.3.4 and analyzing them by means of confocal Raman microscopy (see Fig. S6). We can observe that after 2 min the amount of formed struvite is negligible, whereas after 30 min this phase starts to form, consistently with the decrease in pH. The comparison of the pH profile of B0 and B10 shows that in the presence of borax the decrease in pH is delayed, making easy to relate this effect with the retarding one.

In the following stage of the process, *i.e.,* after about 5 h for B0 and 8 h for B10, the pH slowly begins to rise up to a constant value (8.2 for B0 and 8.9 for B10). We hypothesize that in this stage the pH is controlled by TMP/struvite crystals that are present in the suspension, which result in an alkalization of the aqueous medium in which they are incubated. To demonstrate that, we measured the pH of a suspension containing 0.3 g of TMP and 3 mL of water (same TMP/water ratio as that used for the pH experiment), obtaining a value of pH = 9.5. An analogous experiment was conducted measuring the pH of a struvite dispersion (see struvite synthesis protocol in the Supplementary Material), which also resulted in a pH = 9.5.

It is worth mentioning that, compared to other cements [5,54], the lower pH value of these TMP-based systems could be advantageous for radioactive waste storage applications, where pH < 11 is required [22,23].

3.2. Characterization of set cements

The effect of borax on the microstructure and on the nature and amount of phases formed in set cements was evaluated by comparing B0 and B10 properties determined by means of a multi-technique approach. The phases present in the set samples were first analyzed by means of XRD and FE-SEM; the results obtained are reported in Fig. 5. XRD patterns of samples B0 and B10 (see Fig. 5A) resemble each other and mainly consist of diffraction peaks from struvite and farringtonite (*i.e.*, TMP, see also Fig. S7). The only difference that can be appreciated if closely looking at the diffractograms (Fig. S8) is the presence of a very small amount of newberyite in sample B0, already evidenced by confocal Raman analysis.

We can hypothesize that the lack of newberyite in sample B10 is due to the higher pH in the early stages of setting (see Fig. 4) that affects phosphate speciation, promoting the formation of PO_4^{3-} species over HPO_4^{2-}. For this reason, newberyite ($MgHPO_4{\cdot}3H_2O$) formation may not occur. Interestingly, thermodynamic simulation studies support the absence of newberyite formation in MgO-based cements when borax is present in the mixture [6]. Moreover, in the diffractogram of B10, very small peaks ascribable to unreacted borax are also present (see Fig. S8).

FE-SEM images (Fig. 5B) confirm the similarity of B0 and B10 after setting. The samples are heterogeneous and in their SEM images it is possible to mainly recognize struvite crystals, characterized by a prismatic elongated structure with cross-shaped and Y-shaped cracks, indicated by blue arrows in Fig. 5B [55,56], and few crystals of farringtonite (TMP), appearing as smooth micrometric objects highlighted by red arrows. As a comparison, Fig. S9 in the Supplementary Material shows the morphology of the two distinct phases.

We could gain detailed information on the phosphorus and boron containing phases in both set samples B0 and B10 by exploiting ^{31}P and ^{11}B SS NMR spectroscopy. ^{31}P DE MAS spectra clearly highlight the phosphorus containing phases present, which give rise to peaks at characteristic chemical shifts. Fig. 6 reports the ^{31}P DE MAS spectra of B0 and B10, together with those of TMP, struvite and newberyite, taken as references.

In the spectra of B0 and B10 it is straightforward to recognize the signal of struvite at 6.9 ppm [57–59], and intense peaks at 0.6, −12.6 and −18.8 ppm, also observed in the spectrum of TMP. It must be pointed out that only the signal at 0.6 ppm arises from Tri-Magnesium Phosphate, $Mg_3(PO_4)_2$, while the peaks at −12.6 and −18.8 ppm must be ascribed to different forms of magnesium pyrophosphate ($Mg_2P_2O_7$) and/or metaphosphate [57,60,61]. Moreover, a small signal of newberyite (at −6.8 ppm [59]) is present in the spectrum of B0, in agreement with XRD and Raman results. No signals of DAHP, expected at about 1 ppm [62], are observed in the spectra of B0 and B10, indicating the complete dissolution and consumption of this reactant. The areas underlying the ^{31}P peaks are proportional to the amounts of phosphorus nuclei in the different phases present in the samples, which can be accordingly quantified (Table 2). It can be observed that struvite represents 57 % and 64 % (phases molar percentage) in B0 and B10, respectively, the difference being substantially compensated by newberyite present in B0. It can also be noticed that in TMP $Mg_3(PO_4)_2$ is the sole reacting species (about 50 % of it is consumed in both B0 and B10), as

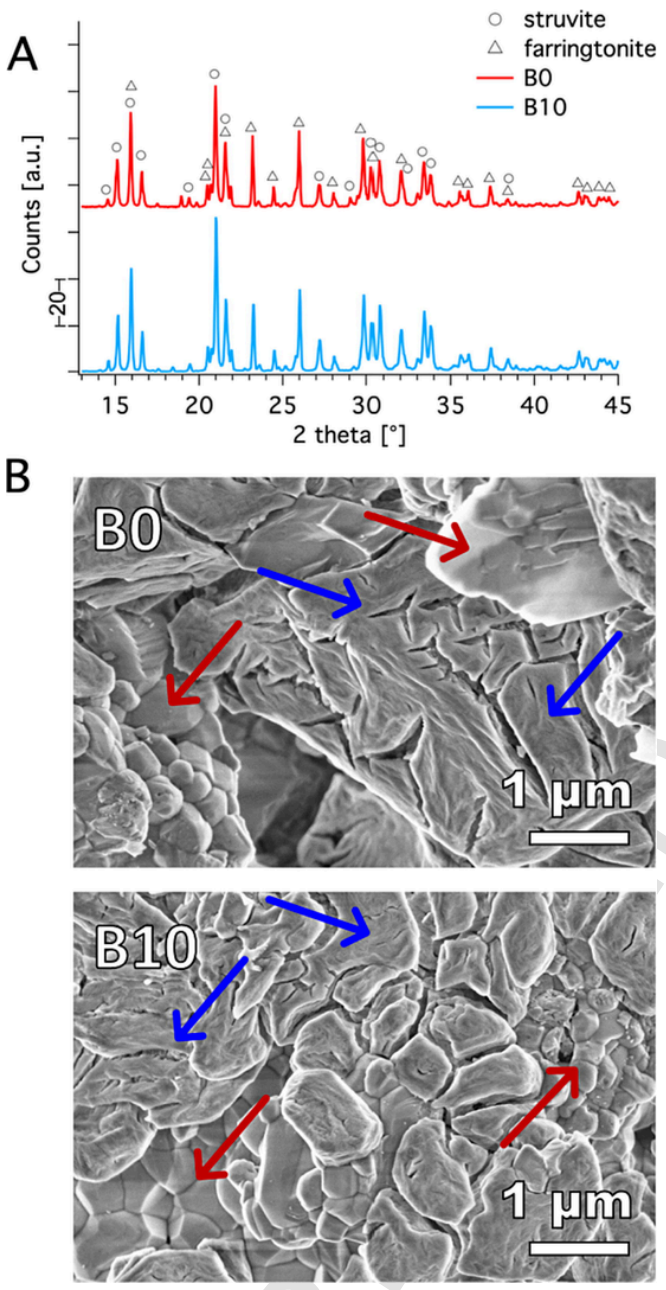

Fig. 5. A) XRD diffractograms and B) FE-SEM images of B0 and B10. Red and blue arrows indicate TMP and struvite crystals, respectively. (For interpretation of the references to colour in this figure legend, the reader is referred to the web version of this article.)

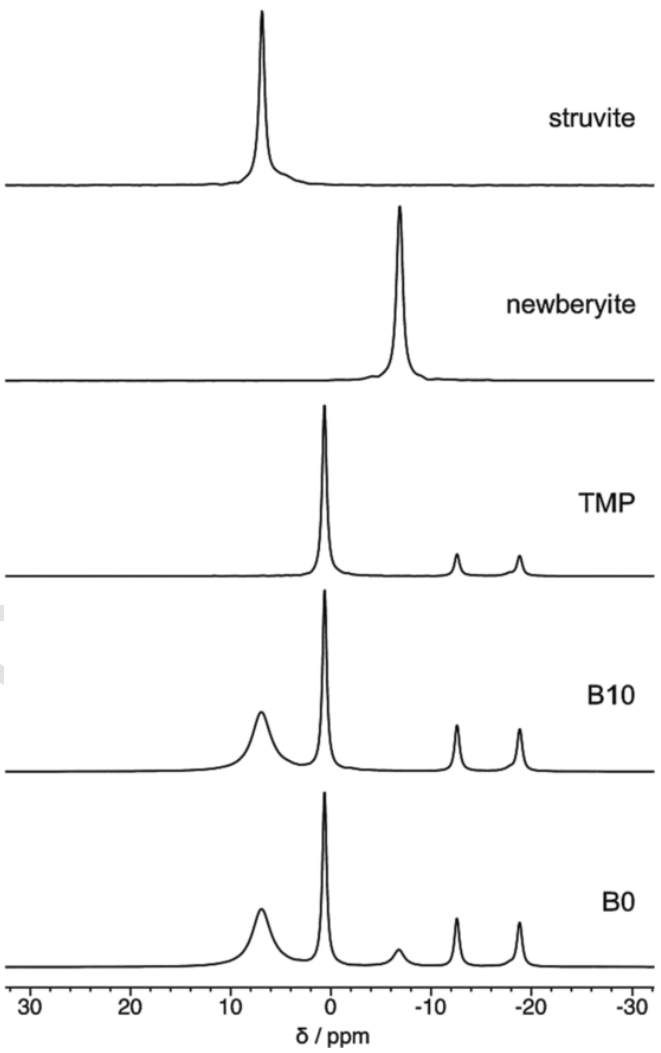

Fig. 6. ^{31}P DE MAS spectra of B0, B10, TMP, newberyite and struvite. The peak of struvite in the spectra of B0 and B10 has a noticeable linewidth due to the reduced ^{1}H decoupling power applied for acquiring the spectra.

Table 2
Relative amounts of the different phosphorus containing phases present in B0 and B10, as obtained from peak areas in quantitative ^{31}P DE MAS spectra. Peak areas were obtained from spectral deconvolution, by considering all isotropic peaks and respective spinning sidebands (Fig. S10).

Sample	$Mg_3(PO_4)_2$ (%)	P2a[a] (%)	P2b[a] (%)	Struvite (%)	Newberyite (%)
B0	19	6	7	57	11
B10	21	7	8	64	0
TMP	75	12	13	–	–

[a] P2a and P2b indicate the species resonating at −12.6 and −18.8 ppm, respectively. For the sake of simplicity, considering that the number of P atoms in metaphosphates is not well defined, for passing from the ^{31}P signal areas to phase percentages we have assumed that both P2a and P2b are pyrophosphate species.

expected. The presence of borax only slightly decreases TMP consumption.

We tried to obtain information on the retarding mechanism of borax in the reaction between TMP and DAHP by looking at the state of boron in the set B10 sample by means of ^{11}B SS NMR.

The ^{11}B SS NMR spectrum of B10, reported in Fig. 7, shows typical signals of boron atoms in BO_4 ($^{[4]}$B) and BO_3 ($^{[3]}$B) moieties: the former give rise to the peaks observed between 0 and 5 ppm, the latter to the broad signal centered at about 14 ppm [63–65]. Since ^{11}B is a quadrupolar nucleus, the signals observed are determined by both chemical shielding and quadrupolar interaction. The latter interaction is relatively small for boron nuclei in highly symmetric (near-tetrahedral geometry) $^{[4]}$B sites, while it is larger and evident in the lineshape of the signals of boron nuclei in less symmetric (trigonal planar geometry) $^{[3]}$B sites. Through a suitable spectral simulation [50], we could determine the chemical shift of $^{[4]}$B ($^{[4]}B_A$, $^{[4]}B_B$, $^{[4]}B_C$, $^{[4]}B_D$) and $^{[3]}$B ($^{[3]}B_A$, $^{[3]}B_B$) sites, the quadrupolar parameters of $^{[3]}$B sites, and the relative amounts of the different sites in B10. The results are reported in Table 3.

The spectral analysis reveals the presence of a large amount (63 % of boron atoms) of borax, which is responsible for signals of $^{[4]}B_D$ and $^{[3]}B_B$ [64,65]. This is in very good agreement with the solubility of borax at pH = 9 (measured in B10), reported to be 5.5/100 (g borax/g

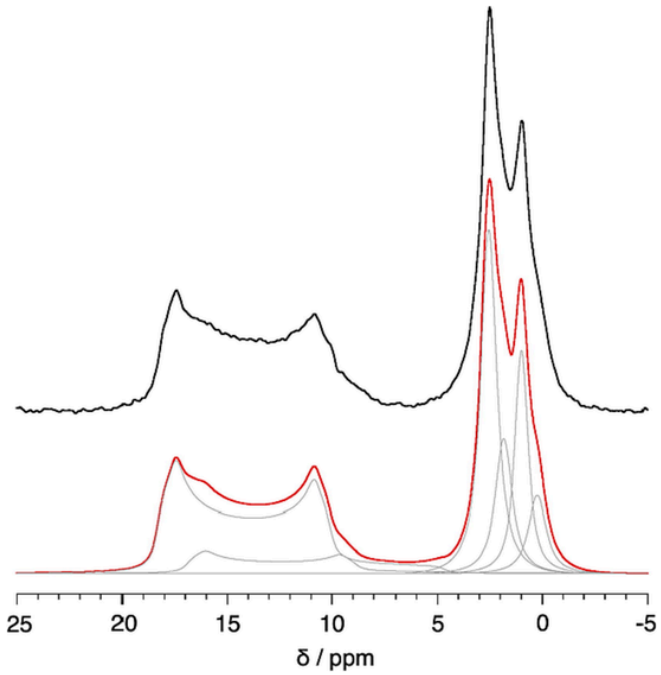

Fig. 7. Experimental (black) and simulated (red) ^{11}B DE MAS spectrum of B10. Gray peaks in the simulated spectrum are the signals corresponding to the different boron sites. (For interpretation of the references to colour in this figure legend, the reader is referred to the web version of this article.)

Table 3
Quadrupolar and chemical shift parameters, and relative amounts of $^{[4]}$B and $^{[3]}$B ^{11}B sites in sample B10, as obtained from spectral simulation.

	$^{[4]}B_A$ [a]	$^{[4]}B_B$ [a]	$^{[4]}B_C$ [a]	$^{[4]}B_D$ [a]	$^{[3]}B_A$	$^{[3]}B_B$
δ_{iso} (ppm)	0.5	1.2	2.1	2.8	18.6	20.1
C_Q (MHz)	0.5[a]	0.5 [a]	0.5 [a]	0.5 [a]	2.48	2.52
H	0.65 [a]	0.65 [a]	0.65 [a]	0.65 [a]	0.1	0.1
I (%)	6	13	10	24	8	39

[a] C_Q and η values of $^{[4]}$Q sites were fixed at the values reported in Ref. [64], since the isotropic shape of the signals did not allow for a reliable determination of these parameters.

water) [66] and corresponding to 37 % of boron atoms. Thus, the observed $^{[4]}B_D$ and $^{[3]}B_B$ signals can be assigned to borax that remains undissolved in the reaction mixture. On the contrary, the other peaks observed must be ascribed to boron species that form and precipitate during the cement reaction and setting, which can give us information on the retarding mechanism of borax. At pH = 9, borax hydrolysis is expected to give rise to various species: $B(OH)_4^-$ and tetraborate B_4^{2-} ($[B_4O_5(OH)_4]^{2-}$) are the most abundant, but also minor amounts of triborates B_3^-/B_3^{2-} ($B_3O_3(OH)_4^-/B_3O_3(OH)_5^{2-}$) and boric acid ($B(OH)_3$) form [67]. These anions, as already reported in reference [40], can interact with Mg^{2+} and, in our case, NH_4^+ cations, abundant in the reaction mixture, forming borates and polyborates that would give rise to the $^{[3]}$B and $^{[4]}$B signals observed. Considering the low w/c ratio and the large amount of unreacted TMP and borax, it is likely that these species locally precipitate at the surface of reactants, rather than forming crystalline phases (indeed they are not observed with XRD). The chemical shift and quadrupolar parameters here found are in qualitative agreement with values reported in the literature for Mg^{2+} and NH_4^+ borates and polyborates [68–70]. Considering the Raman and pH measurement results, which clearly indicate that the effect of borax is to retard the conversion of TMP to struvite and that this is paralleled by a longer persistence of basic pH (9), it can be hypothesized that borax preferentially captures NH_4^+ ions. This phenomenon and the precipitation of these species on the surface of reactants can be thus hypothesized to be the main responsible of retardation. It must be mentioned that Lahalle *et al.* [40], monitoring the hydration of magnesium potassium phosphate cements and investigating the retarding effect of boric acid by means of ^{11}B and ^{31}P SS NMR, observed a $^{[3]}$B signal ascribed to magnesium borate phases, and several $^{[4]}$B signals, most of them with a negative chemical shift and correlating with ^{31}P signals, which were assigned to borates bonded to phosphates, whose precipitation contributed to retardation. In our case, the absence of the corresponding signals in the ^{31}P SS NMR spectrum of B10, suggests that, when borax and TMP are used, the precipitation of borate-phosphates, as well as of Lünebergite [28], would not play a significant role in retarding cement hydration.

Set cements were also investigated in terms of compressive strength, to evaluate the effect of borax on the mechanical performances of the materials. According to the results (see Fig. S11), borax has very little effect on the compressive strength of MPCs, as we obtained 48 ± 7 MPa for B0 and 40 ± 5 MPa for B10. It is worth mentioning that, if needed, the mechanical properties of MPCs might be improved by using reinforcing additives, such as fibers and nanotubular materials [56,71–76].

3.3. Release of boron

In order to evaluate the amount of boron released from the cements upon contact with water, ICP-OES measurements were carried out on sample B10 after incubation in water (see Section 2.4). The result of the test reported in Fig. S12 shows that boron is released from the cement, reaching a constant amount after about 200 h. After this time, no further release is observed. At this stage, the amount of released boron corresponds to about 40 % of that present in the formulation, and it is likely due to the dissolution of a part of unreacted borax, which was already detected in NMR experiments. It is thus possible to hypothesize that only B atoms resulting from the dissolution of excess borax are released from the cement, while those forming BO_3 and BO_4 species with Mg^{2+} and NH_4^+ are likely retained in the cementitious matrix. This highlights the importance of tuning the amount of borax according to the application envisaged for cements, especially in the biomedical field, given the recently raised toxicity issues [44]. Nonetheless, the B released in the investigated conditions corresponds to a borax concentration of 0.12 %, way below the allowed concentration limit of 8.5 % [44].

4. Conclusions

In this work we investigated for the first time the effect of borax as a retarder for TMP-based MPCs. Cements were prepared by reacting TMP and DAHP in the presence of different amounts of borax (2 %, 5 % and 10 % with respect to TMP weight). The setting kinetics was examined by means of Gillmore tests and calorimetry measurements, which demonstrate that borax has a remarkable retarding effect, prolonging the setting time of the paste (t_2 goes from 15 min for B0 to 85 min for B10) and reducing exothermicity (the maximum heat flow value reached is ~ 0.15 W/g for B0 vs ~ 0.02 W/g for B10). This effect is related to a delay in struvite formation, as confirmed by observing struvite's peak evolution in the pastes by means of confocal Raman microscopy and by the pH modifications occurring later in time when borax is present.

The set cements were analyzed to understand how borax is included in the cement matrix by means of XRD, FE-SEM and SS NMR. ^{31}P SS NMR spectra showed that the addition of borax leads to a higher amount of formed struvite at the expense of newberyite, in agreement with XRD. The fate of borax during the hydration was investigated by analyzing the ^{11}B SS NMR spectrum of sample B10. Signals arising from B atoms in different BO_4 and BO_3 moieties were identified and quantified, indicating that both unreacted borax and complexes with ammo-

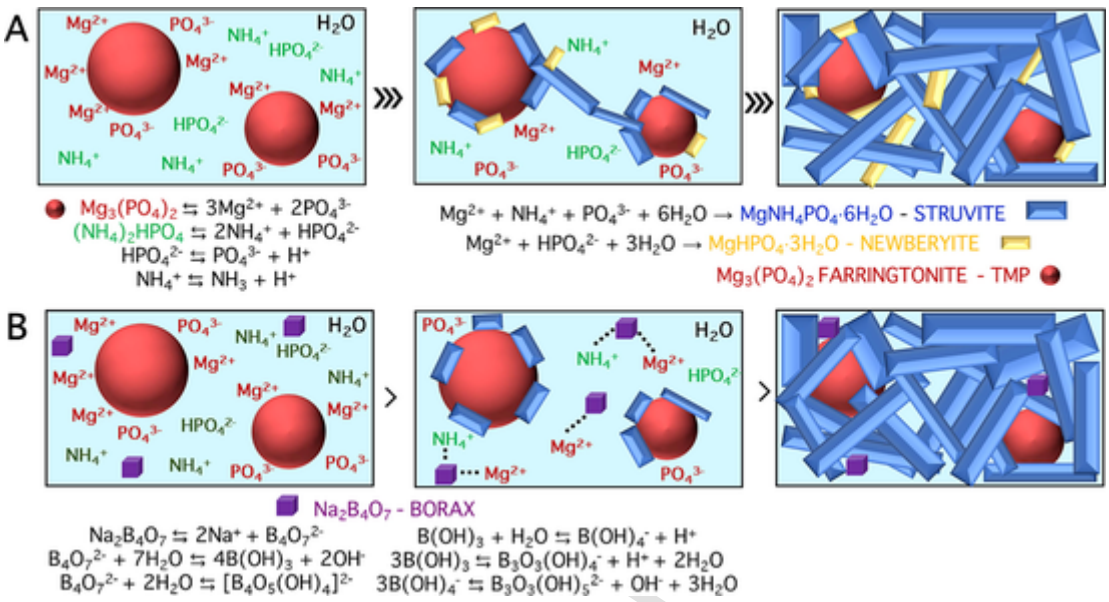

Fig. 8. Hypothesized reaction mechanism for TMP based MPCs in the absence (A) and in the presence (B) of borax, with the possible speciation of ions taking part to the reaction.

nium and magnesium ions are present in the cement, while phases containing B—O—P bonds are not observed.

The setting reaction mechanism is depicted in Fig. 8. In the absence of borax (Fig. 8A), DAHP quickly reacts with Mg^{2+} on the surface of TMP grains, resulting in struvite and few newberyite crystals that entangle and form the cement matrix. When borax is added (Fig. 8B), this process is slowed down due to the interaction of borate species with Mg^{2+} and NH_4^+.

We also evidenced that the unreacted borax might be released upon incubation of the cement in water, highlighting the importance of its fine tuning in the cement formulation, especially in the biomedical field.

The results reported in this work might be useful to prepare TMP-based MPCs with a specific setting time by tuning borax amount. Moreover, the combination of confocal Raman and SS NMR techniques here used could be exploited to investigate the role of borax also in MgO-based MPCs.

CRediT authorship contribution statement

Rita Gelli : Conceptualization, Methodology, Investigation, Writing – original draft, Writing – review & editing, Visualization. **Monica Tonelli :** Conceptualization, Methodology, Investigation, Writing – original draft, Writing – review & editing, Visualization. **Francesca Martini :** Conceptualization, Methodology, Formal analysis, Writing – original draft, Writing – review & editing, Visualization. **Lucia Calucci :** Conceptualization, Methodology, Investigation, Writing – review & editing, Visualization. **Silvia Borsacchi :** Conceptualization, Methodology, Investigation, Resources, Writing – review & editing, Funding acquisition. **Francesca Ridi :** Conceptualization, Methodology, Resources, Writing – review & editing, Funding acquisition.

Declaration of Competing Interest

The authors declare that they have no known competing financial interests or personal relationships that could have appeared to influence the work reported in this paper.

Data availability

Data will be made available on request.

Acknowledgements

The CSGI Consortium and MUR-Italy ("Progetto Dipartimenti di Eccellenza 2018-2022" allocated to Department of Chemistry "Ugo Schiff") are gratefully acknowledged for financial support. This research was also funded by the EU project Horizon 2020 "InnovaConcrete", grant Agreement number 760858. Enzo Barlacchi from the "Laboratorio Prove Strutture e Materiali" of the Department of Civil and Environmental Engineering (DICEA), University of Florence, is acknowledged for the compressive strength measurements. Prof. Mirko Severi is acknowledged for ICP-OES measurements.

CISUP (Centre for Instrument Sharing-University of Pisa) is acknowledged for the use of the Bruker Avance NEO 500 Solid State NMR spectrometer.

Appendix A. Supplementary data

Supplementary data to this article can be found online at https://doi.org/10.1016/j.conbuildmat.2022.128686.

References

[1] M.A. Haque, B. Chen, Research progresses on magnesium phosphate cement: A review, Constr. Build. Mater. 211 (2019) 885–898, https://doi.org/10.1016/j.conbuildmat.2019.03.304.

[2] H. Zhou, B. Liang, H. Jiang, Z. Deng, K. Yu, Magnesium-based biomaterials as emerging agents for bone repair and regeneration: from mechanism to application, J. Magnesium Alloys 9 (3) (2021) 779–804, https://doi.org/10.1016/j.jma.2021.03.004.

[3] M. Nabiyouni, T. Brückner, H. Zhou, U. Gbureck, S.B. Bhaduri, Magnesium-based bioceramics in orthopedic applications, Acta Biomater. 66 (2018) 23–43, https://doi.org/10.1016/j.actbio.2017.11.033.

[4] N. Ostrowski, A. Roy, P.N. Kumta, Magnesium phosphate cement systems for hard tissue applications: A review, ACS Biomater. Sci. Eng. 2 (2016) 1067–1083, https://doi.org/10.1021/acsbiomaterials.6b00056.

[5] S.A. Walling, J.L. Provis, Magnesia-based cements: A journey of 150 years, and cements for the future? Chem. Rev. 116 (2016) 4170–4204, https://doi.org/10.1021/acs.chemrev.5b00463.

[6] W. Han, H. Chen, X. Li, T. Zhang, Thermodynamic modeling of magnesium ammonium phosphate cement and stability of its hydration products, Cem. Concr. Res. 138 (2020) 106223, https://doi.org/10.1016/j.cemconres.2020.106223.

[7] C. Großardt, A. Ewald, L.M. Grover, J.E. Barralet, U. Gbureck, Passive and active

in vitro resorption of calcium and magnesium phosphate cements by osteoclastic cells, Tissue Eng. Part A 16 (2010) 3687–3695, https://doi.org/10.1089/ten.tea.2010.0281.
[8] U. Klammert, E. Vorndran, T. Reuther, F.A. Müller, K. Zorn, U. Gbureck, Low temperature fabrication of magnesium phosphate cement scaffolds by 3D powder printing, J. Mater. Sci. - Mater. Med. 21 (2010) 2947–2953, https://doi.org/10.1007/s10856-010-4148-8.
[9] A. Ewald, K. Helmschrott, G. Knebl, N. Mehrban, L.M. Grover, U. Gbureck, Effect of cold-setting calcium- and magnesium phosphate matrices on protein expression in osteoblastic cells, J. Biomed. Mater. Res. 96B (2011) 326–332, https://doi.org/10.1002/jbm.b.31771.
[10] B. Kanter, M. Geffers, A. Ignatius, U. Gbureck, Control of in vivo mineral bone cement degradation, Acta Biomater. 10 (2014) 3279–3287, https://doi.org/10.1016/j.actbio.2014.04.020.
[11] A. Ewald, B. Lochner, U. Gbureck, J. Groll, R. Krüger, Structural optimization of macroporous magnesium phosphate scaffolds and their cytocompatibility, Key Eng. Mater. 493–494 (2012) 813–819, https://doi.org/10.4028/www.scientific.net/KEM.493-494.813.
[12] N. Ostrowski, B. Lee, D. Hong, P.N. Enick, A. Roy, P.N. Kumta, Synthesis, osteoblast, and osteoclast viability of amorphous and crystalline Tri-Magnesium Phosphate, ACS Biomater. Sci. Eng. 1 (2015) 52–63, https://doi.org/10.1021/ab500073c.
[13] B. Kanter, A. Vikman, T. Brückner, M. Schamel, U. Gbureck, A. Ignatius, Bone regeneration capacity of magnesium phosphate cements in a large animal model, Acta Biomater. 69 (2018) 352–361, https://doi.org/10.1016/j.actbio.2018.01.035.
[14] P. Heilig, P. Sandner, M.C. Jordan, R.G. Jakubietz, R.H. Meffert, U. Gbureck, S. Hoelscher-Doht, Experimental drillable magnesium phosphate cement Is a promising alternative to conventional bone cements, Materials 14 (8) (2021), https://doi.org/10.3390/ma14081925.
[15] R. Gelli, G. Di Pompo, G. Graziani, S. Avnet, N. Baldini, P. Baglioni, F. Ridi, Unravelling the effect of citrate on the features and biocompatibility of magnesium phosphate-based bone cements, ACS Biomater. Sci. Eng. 6 (2020) 5538–5548, https://doi.org/10.1021/acsbiomaterials.0c00983.
[16] E. Vorndran, K. Wunder, C. Moseke, I. Biermann, F.A. Müller, K. Zorn, U. Gbureck, Hydraulic setting $Mg_3(PO_4)_2$ powders for 3D printing technology, Adv. Appl. Ceram. 110 (2011) 476–481, https://doi.org/10.1179/1743676111Y.0000000030.
[17] J. Lee, M.M. Farag, E.K. Park, J. Lim, H. Yun, A simultaneous process of 3D magnesium phosphate scaffold fabrication and bioactive substance loading for hard tissue regeneration, Mater. Sci. Eng. C 36 (2014) 252–260, https://doi.org/10.1016/j.msec.2013.12.007.
[18] J.-A. Kim, J. Lim, R. Naren, H. Yun, E.K. Park, Effect of the biodegradation rate controlled by pore structures in magnesium phosphate ceramic scaffolds on bone tissue regeneration in vivo, Acta Biomater. 44 (2016) 155–167, https://doi.org/10.1016/j.actbio.2016.08.039.
[19] J.A. Kim, H. Yun, Y.-A. Choi, J.-E. Kim, S.-Y. Choi, T.-G. Kwon, Y.K. Kim, T.-Y. Kwon, M.A. Bae, N.J. Kim, Y.C. Bae, H.-I. Shin, E.K. Park, Magnesium phosphate ceramics incorporating a novel indene compound promote osteoblast differentiation in vitro and bone regeneration in vivo, Biomaterials 157 (2018) 51–61, https://doi.org/10.1016/j.biomaterials.2017.11.032.
[20] F. Qiao, C.K. Chau, Z. Li, Property evaluation of magnesium phosphate cement mortar as patch repair material, Constr. Build. Mater. 24 (2010) 695–700, https://doi.org/10.1016/j.conbuildmat.2009.10.039.
[21] Z. Ding, Z. Li, Effect of aggregates and water contents on the properties of magnesium phospho-silicate cement, Cem. Concr. Compos. 27 (2005) 11–18, https://doi.org/10.1016/j.cemconcomp.2004.03.003.
[22] T. Zhang, J. Zou, B. Wang, Z. Wu, Y. Jia, C.R. Cheeseman, Characterization of magnesium silicate hydrate (MSH) gel formed by reacting MgO and silica fume, Materials 11 (2018) 909, https://doi.org/10.3390/ma11060909.
[23] M. Tonelli, F. Martini, L. Calucci, E. Fratini, M. Geppi, F. Ridi, S. Borsacchi, P. Baglioni, Structural characterization of magnesium silicate hydrate: towards the design of eco-sustainable cements, Dalton Trans. 45 (2016) 3294–3304, https://doi.org/10.1039/C5DT03545G.
[24] Y. Li, G. Zhang, D. Hou, Z. Wang, Nanoscale insight on the initial hydration mechanism of magnesium phosphate cement, Constr. Build. Mater. 276 (2021) 122213, https://doi.org/10.1016/j.conbuildmat.2020.122213.
[25] M. Le Rouzic, T. Chaussadent, G. Platret, L. Stefan, Mechanisms of k-struvite formation in magnesium phosphate cements, Cem. Concr. Res. 91 (2017) 117–122, https://doi.org/10.1016/j.cemconres.2016.11.008.
[26] E. Soudée, J. Péra, Mechanism of setting reaction in magnesia-phosphate cements, Cem. Concr. Res. 30 (2000) 315–321, https://doi.org/10.1016/S0008-8846(99)00254-9.
[27] B. Xu, B. Lothenbach, A. Leemann, F. Winnefeld, Reaction mechanism of magnesium potassium phosphate cement with high magnesium-to-phosphate ratio, Cem. Concr. Res. 108 (2018) 140–151, https://doi.org/10.1016/j.cemconres.2018.03.013.
[28] A.S. Wagh, S.Y. Jeong, Chemically bonded phosphate ceramics: I, A dissolution model of formation, J. Am. Ceram. Soc. 86 (2003) 1838–1844, https://doi.org/10.1111/j.1151-2916.2003.tb03569.x.
[29] L. Jun, J. Yong-sheng, H. Guodong, J. Cheng, Retardation and reaction mechanisms of magnesium phosphate cement mixed with glacial acetic acid, RSC Adv. 7 (2017) 46852–46857, https://doi.org/10.1039/C7RA08383A.
[30] J. Li, Y. Ji, G. Huang, Z. Xu, G. Yan, Properties and reaction mechanisms of magnesium phosphate cement mixed with acetic acid, KSCE J. Civ. Eng. 22 (2018) 231–235, https://doi.org/10.1007/s12205-017-1408-x.
[31] X. Wu, H. Dai, S. Yu, Y. Zhao, Y. Long, W. Li, J. Tu, Magnesium calcium phosphate cement incorporating citrate for vascularized bone regeneration, ACS Biomater. Sci. Eng. 6 (2020) 6299–6308, https://doi.org/10.1021/acsbiomaterials.0c00929.
[32] B.E.I. Abdelrazig, J.H. Sharp, B. El-Jazairi, The microstructure and mechanical properties of mortars made from magnesia-phosphate cement, Cem. Concr. Res. 19 (1989) 247–258, https://doi.org/10.1016/0008-8846(89)90089-6.
[33] D.A. Hall, R. Stevens, B. El-Jazairi, The effect of retarders on the microstructure and mechanical properties of magnesia–phosphate cement mortar, Cem. Concr. Res. 31 (2001) 455–465, https://doi.org/10.1016/S0008-8846(00)00501-9.
[34] R. Liu, Y. Yang, S. Sun, Effect of M/P and borax on the hydration properties of magnesium potassium phosphate cement blended with large volume of fly ash, J. Wuhan Univ. Technol.-Mat. Sci. Edit. 33 (2018) 1159–1167, https://doi.org/10.1007/s11595-018-1948-z.
[35] C. Ma, F. Wang, H. Zhou, Z. Jiang, W. Ren, Y. Du, Effect of early-hydration behavior on rheological properties of borax-admixed magnesium phosphate cement, Constr. Build. Mater. 283 (2021) 122701, https://doi.org/10.1016/j.conbuildmat.2021.122701.
[36] C. You, J. Qian, J. Qin, H. Wang, Q. Wang, Z. Ye, Effect of early hydration temperature on hydration product and strength development of magnesium phosphate cement (MPC), Cem. Concr. Res. 78 (2015) 179–189, https://doi.org/10.1016/j.cemconres.2015.07.005.
[37] G. Mestres, M.-P. Ginebra, Novel magnesium phosphate cements with high early strength and antibacterial properties, Acta Biomater. 7 (2011) 1853–1861, https://doi.org/10.1016/j.actbio.2010.12.008.
[38] N. Yang, C. Shi, J. Yang, Y. Chang, Research progresses in magnesium phosphate cement-based materials, J. Mater. Civ. Eng. 26 (2014), https://doi.org/10.1061/(ASCE)MT.1943-5533.0000971.
[39] T. Sugama, L.E. Kukacka, Characteristics of magnesium polyphosphate cements derived from ammonium polyphosphate solutions, Cem. Concr. Res. 13 (1983) 499–506, https://doi.org/10.1016/0008-8846(83)90008-X.
[40] H. Lahalle, C. Cau Dit Coumes, C. Mercier, D. Lambertin, C. Cannes, S. Delpech, S. Gauffinet, Influence of the w/c ratio on the hydration process of a magnesium phosphate cement and on its retardation by boric acid, Cem. Concr. Res. 109 (2018) 159–174, https://doi.org/10.1016/j.cemconres.2018.04.010.
[41] J. Yang, C. Qian, Effect of borax on hydration and hardening properties of magnesium and potassium phosphate cement pastes, J. Wuhan Univ. Technol.-Mat. Sci. Edit. 25 (2010) 613–618, https://doi.org/10.1007/s11595-010-0055-6.
[42] C. Moseke, V. Saratsis, U. Gbureck, Injectability and mechanical properties of magnesium phosphate cements, J. Mater. Sci. Mater. Med. 22 (2011) 2591–2598, https://doi.org/10.1007/s10856-011-4442-0.
[43] T. Christel, S. Christ, J.E. Barralet, J. Groll, U. Gbureck, M.-P. Ginebra, Chelate bonding mechanism in a novel magnesium phosphate bone cement, J. Am. Ceram. Soc. 98 (3) (2015) 694–697, https://doi.org/10.1111/jace.13491.
[44] European Commission. Directorate-General for Health and Consumers, Opinion on Boron compounds, European Commission, BE, 2010. https://data.europa.eu/doi/10.2772/25594.
[45] M. Tonelli, F. Martini, A. Milanesi, L. Calucci, M. Geppi, S. Borsacchi, F. Ridi, Effect of phosphate additives on the hydration process of magnesium silicate cements, J. Therm. Anal. Calorim. 138 (2019) 3311–3321, https://doi.org/10.1007/s10973-019-08847-9.
[46] F. Martini, S. Borsacchi, G. Barcaro, M. Caporali, M. Vanni, M. Serrano-Ruiz, M. Geppi, M. Peruzzini, L. Calucci, Phosphorene and black phosphorus: The ^{31}P NMR view, J. Phys. Chem. Lett. 10 (2019) 5122–5127, https://doi.org/10.1021/acs.jpclett.9b01788.
[47] R. Gelli, L. Mati, F. Ridi, P. Baglioni, Tuning the properties of magnesium phosphate-based bone cements: Effect of powder to liquid ratio and aqueous solution concentration, Mater. Sci. Eng. C 95 (2019) 248–255, https://doi.org/10.1016/j.msec.2018.10.083.
[48] J. Hövelmann, T.M. Stawski, R. Besselink, H.M. Freeman, K.M. Dietmann, S. Mayanna, B.R. Pauw, L.G. Benning, A template-free and low temperature method for the synthesis of mesoporous magnesium phosphate with uniform pore structure and high surface area, Nanoscale 11 (2019) 6939–6951, https://doi.org/10.1039/C8NR09205B.
[49] T. Zhang, C.R. Cheeseman, L.J. Vandeperre, Development of low pH cement systems forming magnesium silicate hydrate (M-S-H), Cem. Concr. Res. 41 (2011) 439–442, https://doi.org/10.1016/j.cemconres.2011.01.016.
[50] D. Massiot, F. Fayon, M. Capron, I. King, S. Le Calvé, B. Alonso, J.-O. Durand, B. Bujoli, Z. Gan, G. Hoatson, Modelling one- and two-dimensional solid-state NMR spectra, Magn. Reson. Chem. 40 (2002) 70–76, https://doi.org/10.1002/mrc.984.
[51] H. Lahalle, C. Cauditcoumes, D. Lambertin, C. Cannes, S. Delpech, S. Gauffinet, Influence of boric acid on the hydration of magnesium phosphate cement at an early age, in: Cea-02509270, 2015. https://hal-cea.archives-ouvertes.fr/cea-02509270.
[52] J. Isac-García, J.A. Dobado, F.G. Calvo-Flores, H. Martínez-García, Green Chemistry Experiments, in: Experimental Organic Chemistry, Elsevier, 2016: pp. 417–484. doi: 10.1016/B978-0-12-803893-2.50013-9.
[53] E. Königsberger, L. Königsberger, eds., Biomineralization: medical aspects of solubility, J. Wiley, Chichester, England; Hoboken, NJ, 2006.
[54] K. Liu, S. Ma, Z. Zhang, F. Han, Hydration and properties of magnesium potassium phosphate cement modified by granulated blast-furnace slag: influence of fineness, Materials 15 (2022) 918, https://doi.org/10.3390/ma15030918.
[55] H. Li, S.-H. Yu, Q.-Z. Yao, G.-T. Zhou, S.-Q. Fu, Chemical control of struvite scale by a green inhibitor polyaspartic acid, RSC Adv. 5 (2015) 91601–91608, https://doi.org/10.1039/C5RA17149K.
124056, https://doi.org/10.1016/j.conbuildmat.2021.124056.
[57] S.N. Scrimgeour, J.A. Chudek, C.H. Lloyd, The determination of phosphorus

containing compounds in dental casting investment products by ^{31}P solid-state MAS-NMR spectroscopy, Dent. Mater. 23 (2007) 415–424, https://doi.org/10.1016/j.dental.2006.02.010.
[58] L.J. Gardner, S.A. Walling, S.M. Lawson, S. Sun, S.A. Bernal, C.L. Corkhill, J.L. Provis, D.C. Apperley, D. Iuga, J.V. Hanna, N.C. Hyatt, Characterization of and structural insight into struvite-K, $MgKPO_4{\cdot}6H_2O$, an analogue of struvite, Inorg. Chem. 60 (2021) 195–205, https://doi.org/10.1021/acs.inorgchem.0c02802.
[59] N. Ma, A.A. Rouff, B.L. Phillips, A ^{31}P NMR and TG/DSC-FTIR Investigation of the influence of initial pH on phosphorus recovery as struvite, ACS Sustainable Chem. Eng. 2 (2014) 816–822, https://doi.org/10.1021/sc4004746.
[60] A. Sut, S. Greiser, C. Jäger, B. Schartel, Interactions in multicomponent flame-retardant polymers: Solid-state NMR identifying the chemistry behind it, Polym. Degrad. Stab. 121 (2015) 116–125, https://doi.org/10.1016/j.polymdegradstab.2015.08.018.
[61] M.A. Aramendía, V. Borau, C. Jiménez, J.M. Marinas, F.J. Romero, J.R. Ruiz, XRD and solid-state NMR study of magnesium oxide-magnesium orthophosphate systems, J. Solid State Chem. 135 (1) (1998) 96–102, https://doi.org/10.1006/jssc.1997.7602.
[62] P.J. Wilkes, Nmr of phosphorus-containing solids, Doctoral, Durham University, 1987. http://etheses.dur.ac.uk/6666/.
[63] A. Krishnamurthy, T. Nguyen, M. Fayek, B. Shabaga, S. Kroeker, Network structure and dissolution properties of phosphate-doped borosilicate glasses, J. Phys. Chem. C 124 (2020) 21184–21196, https://doi.org/10.1021/acs.jpcc.0c06553.
[64] M.R. Hansen, T. Vosegaard, H.J. Jakobsen, J. Skibsted, ^{11}B chemical shift anisotropies in borates from ^{11}B MAS, MQMAS, and single-crystal NMR spectroscopy, J. Phys. Chem. A 108 (2004) 586–594, https://doi.org/10.1021/jp030939h.
[65] S.F. Dec, G.E. Maciel, High-speed MAS NMR spectra of quadrupolar nuclides at high magnetic fields, J. Magn. Reson. 87 (1990) (1969) 153–159, https://doi.org/10.1016/0022-2364(90)90093-O.
[66] J. Chen, J. Peng, X. Wang, Y. Dong, W.u. Li, Effects of CO_3^{2-} and OH^- on the solubility, metastable zone width and nucleation kinetics of borax decahydrate, R. Soc. open sci. 6 (6) (2019) 181862, https://doi.org/10.1098/rsos.181862.
[67] A.N. Ay, B. Zümreoglu-Karan, A. Temel, L. Mafra, Layered double hydroxides with interlayer borate anions: A critical evaluation of synthesis methodology and pH-independent orientations in nano-galleries, Appl. Clay Sci. 51 (2011) 308–316, https://doi.org/10.1016/j.clay.2010.12.015.
[68] B. Zhou, V.K. Michaelis, Y. Pan, Y. Yao, K.T. Tait, B.C. Hyde, J.E.C. Wren, B.L. Sherriff, S. Kroeker, Crystal structure refinements of borate dimorphs inderite and kurnakovite using ^{11}B and ^{25}Mg nuclear magnetic resonance and DFT calculations, Am. Mineral. 97 (2012) 1858–1865, https://doi.org/10.2138/am.2012.4020.
[69] Ü. Sızır, Ö. Yurdakul, D.A. Köse, F. Akkurt, Novel non-metal cation (NMC) pentaborate salts of some amino acids, Molecules 24 (2019) 2790, https://doi.org/10.3390/molecules24152790.
[70] M.A. Beckett, S.J. Coles, P.N. Horton, C.L. Jones, Polyborate anions partnered with large nonmetal cations: triborate(1–), pentaborate(1–) and heptaborate(2–) salts, Eur. J. Inorg. Chem. 2017 (2017) 4510–4518, https://doi.org/10.1002/ejic.201700551.
[71] H. Feng, G. Chen, D. Gao, K. Zhao, C. Zhang, Mechanical Properties of Steel Fiber-Reinforced Magnesium Phosphate Cement Mortar, Adv. Civil Eng. 2018 (2018) e3978318. doi: 10.1155/2018/3978318.
[72] J. Qin, J. Qian, Z. Li, C. You, X. Dai, Y. Yue, Y. Fan, Mechanical properties of basalt fiber reinforced magnesium phosphate cement composites, Constr. Build. Mater. 188 (2018) 946–955, https://doi.org/10.1016/j.conbuildmat.2018.08.044.
[73] L. Jun, J. Yong-sheng, J. Cheng, X. Zhishan, Improvement and mechanism of the mechanical properties of magnesium ammonium phosphate cement with Chopped fibers, Constr. Build. Mater. 243 (2020) 118262, https://doi.org/10.1016/j.conbuildmat.2020.118262.
[74] Z. Jiang, L. Zhang, T. Geng, Y. Lai, W. Zheng, M. Huang, Study on the compressive properties of magnesium phosphate cement mixing with eco-friendly coir fiber considering fiber length, Materials 13 (2020) 3194, https://doi.org/10.3390/ma13143194.
[75] Y. Li, H. Lin, Experimental study on the effect of different dispersed degrees carbon nanotubes on the modification of magnesium phosphate cement, Constr. Build. Mater. 200 (2019) 240–247, https://doi.org/10.1016/j.conbuildmat.2018.12.113.
[76] Y. Du, J. Yang, B. Skariah Thomas, L. Li, H. Li, W. Mohamed Shaban, W. Tung Chong, Influence of hybrid graphene oxide/carbon nanotubes on the mechanical properties and microstructure of magnesium potassium phosphate cement paste, Constr. Build. Mater. 260 (2020) 120449. doi: 10.1016/j.conbuildmat.2020.120449.